other dislocation reactions cannot be excluded and may also be effective in strengthening. In-depth investigations of the plastic deformation mechanism of the present sample with nano-twins are needed.

The accumulation of dislocation in the sample during plastic deformation is responsible for the obvious work hardening in the tensile stress-strain curve, which may also lead to an increment of resistivity due to more scattering dislocations. The electrical resistivity measurements verified that the room-temperature resistivity was increased by about 11% after the tensile deformation.

References and Notes

1. D. W. Callister Jr., *Materials Science and Engineering, An Introduction* (Wiley, New York, ed. 5, 2000).
2. E. A. Brandes, G. B. Brook, *Smithells Metals Reference Book* (Butterworth-Heinemann, Oxford, 1998).
3. P. V. Anderws, M. B. West, C. R. Robeson, *Philos. Mag.* **19**, 887 (1969).
4. R. H. Pry, R. W. Hennig, *Acta Metall.* **2**, 318 (1954).
5. J. W. Christian, S. Mahajan, *Prog. Mater. Sci.* **39**, 1 (1995).
6. S. D. Dahlgren *et al.*, *Thin Solid Films* **40**, 345 (1977).
7. A. P. Sutton, R. W. Balluffi, *Interfaces in Crystalline Materials* (Clarendon, Oxford, 1995).
8. H. Natter, M. Schmelzer, R. Hempelmann, *J. Mater. Res.* **13**, 1186 (1998).
9. Materials and methods are available as supporting material on *Science* Online.
10. A. A. Rasmussen, J. A. D. Jensen, A. Horsewell, A. J. Somers, *Electrochim. Acta* **47**, 67 (2001).
11. P. G. Sanders, J. A. Eastman, J. R. Weertman, *Acta Mater.* **45**, 4019 (1997).
12. Y. Wang, M. Chen, F. Zhou, E. Ma, *Nature* **419**, 912 (2002).
13. S. S. Brenner, *J. Appl. Phys.* **27**, 1484 (1956).
14. C. C. Koch, D. G. Morris, K. Lu, A. Inoue, *Mater. Res. Soc. Bull.* **24**, 54 (1999).
15. The IACS is material in which the resistance of a wire 1 m in length and weighing 1 g is 0.15328 ohm at 20°C. The electrical conductivity of the coarse-grained OFHC copper at 20°C is 101.5% IACS.
16. Kh. M. Mannan, Kh. R. Karin, *J. Phys. F Metal Phys.* **5**, 1687 (1975).
17. H. Yoshinaga, *Phys. Stat. Sol.* **18**, 625 (1966).
18. I. Nakamichi, *Mat. Sci. Forum* **207-209**, 47 (1996).
19. C. J. Youngdahl, J. R. Weertman, R. C. Hugo, H. H. Kung, *Scripta Mater.* **44**, 1475 (2001).
20. M. A. Meyers, K. K. Chawla, *Mechanical Behavior of Materials* (Prentice Hall, Upper Saddle River, NJ, 1999).

21. The authors thank the National Natural Science Foundation (grants 50021101 and 50201017), the Ministry of Science and Technology of China (grant G1999064505), and the Max-Planck Society of Germany for financial support; X. Si and H. B. Ma for sample preparation; Z. H. Jin and B. Wu for discussions and TEM experiments; and X. N. Jing for electrical resistivity measurements.

Supporting Online Material

www.sciencemag.org/cgi/content/full/1092905/DC1
Materials and Methods
Table S1

23 October 2003; accepted 5 March 2004
Published online 18 March 2004;
10.1126/science.1092905
Include this information when citing this paper.

Removal of Meteoric Iron on Polar Mesospheric Clouds

John M. C. Plane,[1]* Benjamin J. Murray,[1] Xinzhao Chu,[2] Chester S. Gardner[2]

Polar mesospheric clouds are thin layers of nanometer-sized ice particles that occur at altitudes between 82 and 87 kilometers in the high-latitude summer mesosphere. These clouds overlap in altitude with the layer of iron (Fe) atoms that is produced by the ablation of meteoroids entering the atmosphere. Simultaneous observations of the Fe layer and the clouds, made by lidar during midsummer at the South Pole, demonstrate that essentially complete removal of Fe atoms can occur inside the clouds. Laboratory experiments and atmospheric modeling show that this phenomenon is explained by the efficient uptake of Fe on the ice particle surface.

Polar mesospheric clouds (PMCs), also commonly known as noctilucent clouds, have been intensively studied in recent years because of their potential to provide an early indication of climate change in the upper atmosphere (*1*), although this remains controversial (*2*). PMCs consist of ice particles that form through the microphysical processes of nucleation, condensation, and sedimentation (*3*). They occur when the temperature drops below the water frost point, which is about 150 K in the upper mesosphere (*4*, *5*). The largest ice particles (radius >20 nm) sediment to the base of the cloud layer, where they scatter light sufficiently strongly to be observed by lidar (*5*, *6*) or even with the naked eye during twilight. The meteoric Fe layer peaks at altitudes around 87 km and has a half-width of about 7 km (*7*). Thus, if the removal of iron species on the ice particles in a PMC is rapid relative to the input of fresh iron from meteoric ablation, the vertical transport of Fe into the cloud via eddy diffusion, and the lifetime of the cloud itself, then a local depletion or "bite-out" in the Fe density profile should result.

The University of Illinois Fe Boltzmann temperature lidar (*8*) was installed at the Amundsen-Scott South Pole Station in 1999. This instrument measures the Fe density between about 75 and 110 km. It consists of two lidars operating at the wavelengths of two closely spaced Fe resonance lines (372 and 374 nm). The lidars measure simultaneously the relative populations of the lowest spin-orbit multiplets of ground-state Fe (*8*). In the presence of a PMC, the lidar return signals consist of resonance backscatter from Fe atoms plus Mie backscatter (the elastic scattering of photons) from the cloud particles. Because the PMC backscatter signals are nearly identical at 372 and 374 nm, whereas the Fe signals are substantially different (the relative population of the higher multiplet is 1.2% at 145 K), the PMC signal can be eliminated from the 372-nm data by subtracting the 374-nm return signal and scaling the difference. The scaling factor was calculated from the known temperature-dependent relationship of the Fe backscatter signals at 372 and 374 nm (*8*), assuming the temperature from a South Pole climatology (*9*). Hence, the Fe density was determined at the altitude of the cloud layer.

Figure 1 shows simultaneous measurements of the atomic Fe and Mie backscatter on 19 January 2000. Note the bite-out in the Fe layer, with essentially complete removal of Fe at the peak of the PMC. These strong bite-outs occur in the period between mid-December and the first week in February, and only when the cloud backscatter brightness exceeds 200 equivalent Fe atoms cm^{-3} (about 10% of the observing time, whereas weaker PMCs are visible for 67% of this period). Another striking feature of the Fe layer in Fig. 1 is that the peak occurs around 92 km, with a density of less than 3000

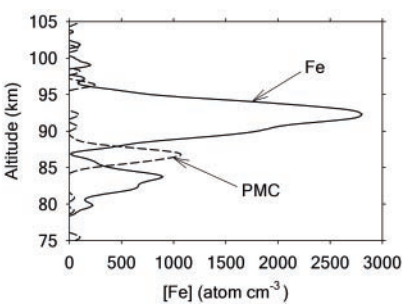

Fig. 1. Simultaneous observations of the atomic Fe density and PMC backscatter signal. The measurements were made with the University of Illinois Fe Boltzmann lidar, operating at 372 and 374 nm, respectively. The signals are averaged between 03:00 and 06:00 UT on 19 January 2000. The PMC backscatter signal is expressed as equivalent Fe atoms cm^{-3} for comparison with the atomic Fe resonance fluorescence signal.

[1]School of Environmental Sciences, University of East Anglia, Norwich NR4 7TJ, UK. [2]Department of Electrical and Computer Engineering, University of Illinois at Urbana-Champaign, Urbana, IL 61801, USA.

*To whom correspondence should be addressed. E-mail: j.plane@uea.ac.uk

cm^{-3}. This situation contrasts with the Fe layer during the last two weeks of February, when only very weak cloud layers are occasionally observed. The layer then peaks between 87 and 89 km, with densities around 2×10^4 cm^{-3}.

To examine whether the Fe layer bite-outs can be explained by the removal of Fe on ice particles, we first performed laboratory experiments to measure the uptake rate of Fe on ice. A fast-flow tube technique (*10*) was used, with Fe atoms generated by pulsed laser ablation of an Fe target (*11*). The uptake coefficient, γ, which is the probability that Fe atoms colliding with the ice surface are permanently removed from the gas phase, was found to be essentially unity on cubic-crystalline ice over the relevant temperature range of 130 to 150 K. The other major iron species in the upper mesosphere/lower thermosphere are predicted to be Fe^+ and FeOH (*12*). Because Fe^+ is charged and FeOH is polar (*11*), they are likely to bind even more strongly than Fe to ice. We therefore assume in the atmospheric model described below that $\gamma = 1$ for all iron species.

The PMC illustrated in Fig. 1 has a peak backscatter of 1050 equivalent Fe atoms cm^{-3}. Figure 2 shows the particle number density that would be required to produce this backscatter, over a range of spherical particle sizes from mode radius $r = 5$ to 100 nm. We assume the particle size to be normally distributed with a standard deviation of $\sim 0.22r$, in accord with a recent cloud microphysics model (*13*). The Mie scattering cross section, calculated for spherical cubic water ice at 130 to 150 K (*14*), is then averaged over this distribution. Figure 2 shows that a small concentration (<10 cm^{-3}) of large particles is required to generate the observed lidar backscatter, whereas more than 10^7 cm^{-3} would be required if $r < 10$ nm. However, such a large number of particles would involve the condensation of a huge quantity of H_2O (mixing ratio > 1000 ppm). The thick black line in Fig. 2 shows the range of particle sizes that involve a realistic H_2O mixing ratio [<15 ppm (*15*)] to produce the observed backscatter. For the light-scattering layer in Fig. 1, the mode radius at the backscatter peak must therefore be at least 44 nm. Also plotted in Fig. 2 is the corresponding Fe uptake rate. This is defined as $0.25\gamma\langle v\rangle A$, where $\langle v\rangle$ is the root-mean-square velocity of Fe atoms and A is the volumetric surface area of the ice particles. Note that the uptake rate decreases by an order of magnitude when r increases from 44 to 100 nm. Therefore, the range of particle sizes that can account for both the observed Fe bite-out and the cloud backscatter is quite constrained.

To model the observations, we used a one-dimensional mesospheric model (*16*) extending from 65 to 110 km with a resolution of 0.5 km. The model uses time-implicit integration (*17*) with a 10-min time step. It contains a full treatment of the odd oxygen and hydrogen chemistry in the mesosphere (*18*) and a recent gas-phase iron chemistry reaction scheme (*12*). The Fe ablation flux was set to 1.1×10^4 atoms cm^{-2} s^{-1} [8% of the iron contained in the estimated interplanetary dust flux at the South Pole of around 60×10^7g day^{-1} (*19*, *20*)] by fitting the model to the observed Fe layer in late February, when PMCs were absent. The meteoric ablation profile is calculated using the standard ablation equations (*21*), with a meteoroid size and velocity distribution from the Long Duration Exposure Facility experiment (*19*). The temperature profiles for January and February are taken from a South Pole climatology (*9*), and the vertical eddy diffusion coefficient is from a global circulation model (*22*).

Figure 3A shows the distributions of ice particle size and number density used to define the PMC in the model. These distributions were adapted from a recent cloud microphysics model (*13*), with two modifications. First, the mode radius was reduced by 10% at all altitudes so as to match the peak Mie backscatter brightness to the lidar measurement. Second, a vertical height shift was applied to the particle number and size distributions. This takes account of the strong upwelling over Antarctica during the austral summer, which causes cloud layers to be about 2 km higher than in the northern high latitudes (*5*). The shift applied in the present model was a constant 2.4 km up to 85.5 km, and then decreased with a scale height of 3 km at higher altitudes.

Figure 3B shows that the predicted backscatter brightness profile agrees well with that observed. Note that the H_2O-ice mixing ratio of the model PMC is 5.7 ppm, in sensible accord with the observed H_2O mixing ratio in the upper mesosphere during summer at high latitudes (*15*). The volumetric surface area of the PMC is also plotted in Fig. 3B. This shows that although A peaks around 86.5 km, there is still some ice surface area at heights well above the altitude at which the cloud is visible by lidar (e.g., at 90 km, A is 10% of the peak), because of the large density of small particles ($r < 15$ nm).

Figure 3C shows the modeled Fe layer at 90°S for two sets of conditions: January with the PMC present as a static layer, and late February in the absence of a cloud. The corresponding lidar measurements are in-

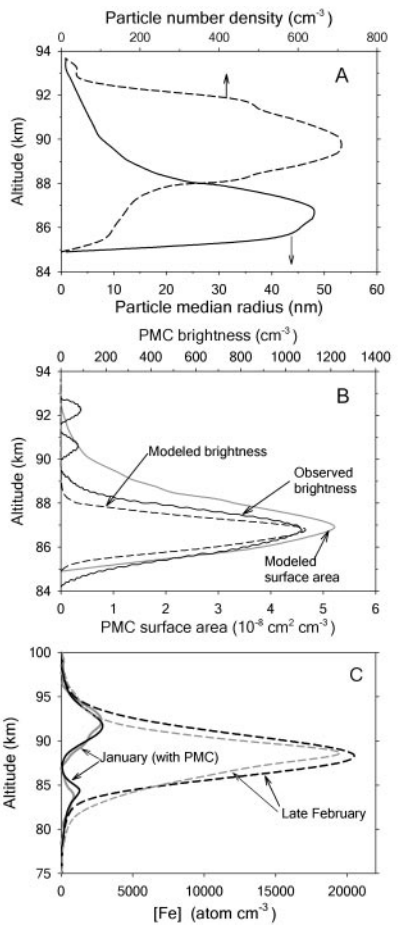

Fig. 3. Modeling the uptake of Fe atoms on a PMC. (**A**) Height distribution of the number density (dashed line) and mode radius (solid line) of ice particles in the PMC used to model the Fe bite-out in Fig. 1. The particle distributions are adapted from a cloud microphysics model (*13*), as described in the text. (**B**) The resulting PMC brightness that would be seen by the lidar at 374 nm, compared with observed brightness. The volumetric surface area of the particle distribution in (A) is also shown. (**C**) A comparison of the modeled (black lines) and observed (gray lines) Fe density profiles at 90°S during January with the PMC in (A), and also in late February with no PMC.

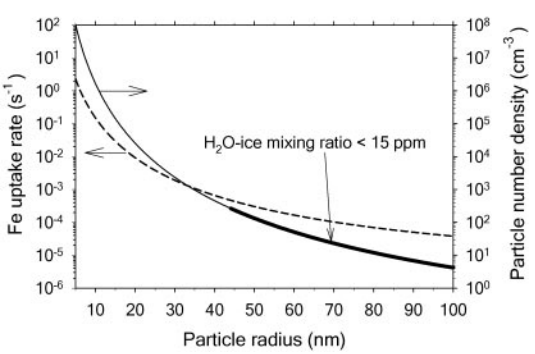

Fig. 2. Particle number density and Fe uptake rate as a function of particle size for a constant PMC brightness. The particle number density, required to generate the peak PMC brightness in Fig. 1, is plotted as a function of particle mode radius (solid line). The resulting dependence of the Fe uptake rate on particle radius is also shown (dashed line). The thick black line indicates the range of particle sizes that involve realistic H_2O mixing ratios (<15 ppm in the upper mesosphere).

cluded for comparison. The model reproduces well the Fe density and lower peak height of the Fe layer during February, establishing that the rates of meteoric ablation and downward transport of Fe species in the model are of the correct magnitude. In addition, the model predicts very satisfactorily the marked bite-out, high peak height, and overall depletion of the layer in the presence of the PMC in January.

When the PMC is turned on in the model, the Fe is depleted most rapidly at the peak of the layer (86.5 km), taking only 2 hours for the Fe to be depleted by a factor e (2.72). Note that this justifies treating the PMC as a static layer in the model, and implies that Fe bite-out should appear whenever a substantial cloud layer forms. Indeed, in the present data set a bite-out is always present when the particle backscatter signal is greater than 200 equivalent Fe atoms cm^{-3}. In contrast, at 91 km the rate of Fe uptake is considerably slower, requiring 31 hours for the Fe to be depleted by a factor e. This is much longer than the 2- to 10-hour periods for which strong PMCs are typically observed. Furthermore, between mid-December and early February the Fe layer is always substantially depleted and peaks above 90 km, irrespective of whether an observable cloud is present. We believe this is strong evidence for a persistent population of small ($r < 15$ nm) ice particles above 86 km over the South Pole during summer, as has been proposed in the high-latitude Arctic (*13*).

We conclude that there is compelling evidence for uptake on ice particles causing the persistent summertime depletion of the meteoric Fe layer at South Pole, and that the bite-outs inside strong PMCs provide a rare example of heterogeneous removal directly observed in the atmosphere. A final point to consider is the fate of the adsorbed iron: Once the cloud sediments or drifts horizontally into a warmer region, the ice particles will sublimate and probably leave behind a concentrated layer of residual iron oxyhydroxide particles.

References and Notes

1. G. E. Thomas, J. Olivero, *Adv. Space Res.* **28**, 937 (2001).
2. U. von Zahn, *Eos* **84**, 261 (2003).
3. G. E. Thomas, *Rev. Geophys.* **29**, 553 (1991).
4. F. J. Lübken, *J. Geophys. Res.* **104**, 9135 (1999).
5. X. Chu, C. S. Gardner, R. G. Roble, *J. Geophys. Res.* **108** (D8), 10.1029/2002JD002524 (2003).
6. G. Hansen, M. Serwazi, U. von Zahn, *Geophys. Res. Lett.* **16**, 1445 (1989).
7. M. Helmer, J. M. C. Plane, J. Qian, C. S. Gardner, *J. Geophys. Res.* **103**, 10913 (1998).
8. X. Z. Chu, W. L. Pan, G. C. Papen, C. S. Gardner, J. A. Gelbwachs, *Appl. Opt.* **41**, 4400 (2002).
9. W. L. Pan, C. S. Gardner, *J. Geophys. Res.* **108** (D18), 10.1029/2002JD003217 (2003).
10. B. J. Murray, J. M. C. Plane, *Phys. Chem. Chem. Phys.* **5**, 4129 (2003).
11. D. E. Self, J. M. C. Plane, *Phys. Chem. Chem. Phys.* **5**, 1407 (2003).
12. J. M. C. Plane, D. E. Self, T. Vondrak, K. R. S. Woodcock, *Adv. Space Res.* **32**, 699 (2003).
13. U. von Zahn, U. Berger, *J. Geophys. Res.* **108** (D7), 10.1029/2002JD002409 (2003).
14. P. J. Espy, H. Jutt, *J. Atmos. Solar-Terr. Phys.* **64**, 1823 (2002).
15. M. McHugh *et al.*, *Geophys. Res. Lett.* **30** (8), 10.1029/2002GL016859 (2003).
16. B. J. Murray, J. M. C. Plane, *Adv. Space Res.* **31**, 2075 (2003).
17. T. Shimazaki, *Minor Constituents in the Middle Atmosphere* (Reidel, Dordrecht, Netherlands, 1985).
18. S. P. Sander *et al.*, *Tech. Rep. 02-25* (Jet Propulsion Laboratory, Pasadena, CA, 2003).
19. N. McBride, S. F. Green, J. A. M. McDonnell, *Adv. Space Res.* **23**, 73 (1999).
20. I. Yrjola, P. Jenniskens, *Astron. Astrophys.* **330**, 739 (1998).
21. D. M. Hunten, R. P. Turco, O. B. Toon, *J. Atmos. Sci.* **37**, 1342 (1980).
22. R. R. Garcia, S. Solomon, *J. Geophys. Res.* **99**, 12937 (1994).

23. The laboratory and modeling work at the University of East Anglia was supported by the Royal Society and the Natural Environmental Research Council. B.J.M. thanks the School of Environmental Sciences for a research studentship. The NSF supported the development and operation of the University of Illinois Fe lidar at the South Pole.

3 November 2003; accepted 8 March 2004

A Functional Protein Chip for Pathway Optimization and in Vitro Metabolic Engineering

Gyoo Yeol Jung and Gregory Stephanopoulos*

Pathway optimization is difficult to achieve owing to complex, nonlinear, and largely unknown interactions of enzymes, regulators, and metabolites. We report a pathway reconstruction using RNA display–derived messenger RNA–enzyme fusion molecules. These chimeras are immobilized by hybridization of their messenger RNA end with homologous capture DNA spotted on a substrate surface. Enzymes thus immobilized retain activity proportional to the amount of capture DNA, allowing modulation of the relative activity of pathway enzymes. Entire pathways can thus be reconstructed and optimized in vitro from genomic information. We provide concept validation with the sequential reactions catalyzed by luciferase and nucleoside diphosphate kinase and further illustrate this method with the optimization of the five-step pathway for trehalose synthesis.

The properties of metabolic pathways uniquely depend on the relative activities of all the enzymes that they comprise. As such, metabolic pathways can be optimized by modulating the relative expression of the corresponding genes. Pathway optimization through the introduction of genetic controls is indeed a central tenet of metabolic engineering (*1*). However, despite recent advances in pathway optimization and metabolic engineering (*2–9*), this remains a demanding task owing to the complexity of metabolic pathways. Methods such as single-gene overexpression or overexpression of all pathway genes are optimal strategies only in special cases. Mathematical methods can aid in pathway optimization provided that satisfactory kinetic models are available. However, their use has been limited owing to the lack of reliable in vivo kinetic models. Hence, pathway optimization must rely on combinatorial experimental methods, whereby the relative amounts (or activities) of the pathway enzymes are altered and the effect on the pathway performance is measured. However, this is difficult to achieve because in general, all pathway enzymes are not available in pure and active form.

mRNA-protein fusions, originally developed for use in RNA display (*10*), are molecules linking covalently an expressed mRNA and its translated protein product. These fusion molecules (fig. S1A) comprise two distinct parts. The mRNA part carries genetic information that can be used as a specific tag to capture the fusion molecule by a homologous capture DNA, and the protein carries potential functionality. If the capture DNA is immobilized on a solid support, it could be used as an anchor for separating the entire chimeric molecule from a mixture of similar molecules and attaching it on the support (fig. S1B).

Weng *et al.* (*11*) demonstrated that mRNA-protein fusion molecules could be hybridized on a DNA microarray to build a protein microarray. Using three different types of proteins and their tagged antibodies, they showed that mRNA-protein fusion molecules could specifically bind to their corresponding capture DNA. We used this platform for catalytically active proteins in order to reconstruct metabolic pathways whose enzymes were not readily available.

Department of Chemical Engineering, Massachusetts Institute of Technology, Room 56-469, Cambridge, MA 02139, USA.

*To whom correspondence should be addressed. E-mail: gregstep@mit.edu